Elastic and inelastic scattering of 240-MeV ^{6}Li ions from ^{40}Ca and ^{48}Ca and tests of a systematic optical potential

Krishichayan, X. Chen,* Y.-W. Lui, J. Button, and D. H. Youngblood
Cyclotron Institute, Texas A&M University, College Station, Texas 77843, USA
(Received 24 February 2010; published 22 April 2010)

Elastic and inelastic scattering of 240-MeV ^{6}Li particles from ^{40}Ca and ^{48}Ca were measured with the multipole-dipole-multipole spectrometer from $4^\circ \leqslant \theta_{\mathrm{c.m.}} \leqslant 40^\circ$. Optical potential parameters were obtained by fitting the elastic-scattering data with the double-folding model using the density-dependent M3Y *NN* effective interaction and $B(E2)$ and $B(E3)$ values obtained for low-lying 2^+ and 3^- states agreed with the adopted values. The results are compared with those obtained using potentials derived from the systematics of potentials previously obtained for ^{24}Mg, ^{28}Si, ^{58}Ni, and ^{90}Zr. Cross sections for excitation of giant resonances were also calculated with the potentials obtained.

DOI: 10.1103/PhysRevC.81.044612 PACS number(s): 25.70.Bc, 24.10.Ht, 27.30.+t, 27.40.+z

I. INTRODUCTION

The properties of the isoscalar giant resonances in nuclei are important because of what they tell us of the bulk nuclear properties. The isoscalar giant monopole resonance (ISGMR) is of particular importance because its energy is related to the nuclear compressibility and from this the compressibility of nuclear matter (K_{nm}) can be obtained. A comparison of the results of systematic studies of the ISGMR in stable nuclei with calculations using the Gogny interaction resulted in the value $K_{nm} = 231 \pm 5$ MeV [1]. Calculations with other interactions and relativistic models have shown that the location of the ISGMR is also sensitive to the symmetry energy and studies of stable Sn isotopes have led to some constraints on K_{sym} [2,3]. In order to determine the contribution from symmetry energy more accurately, a systematic study of the ISGMR over a wide range of *(N-Z)/A* is necessary. This range can be expanded by extending ISGMR measurements to unstable nuclei using inverse reactions.

The inelastic scattering of α particles has been a valuable technique for studying ISGMR in many stable nuclei for several years [1,4,5]. Unfortunately He targets have serious limitations for such studies using inverse reactions. At Riken a liquid He target 120 mg/cm^2 in thickness was employed to study the ISGMR in ^{14}O [6] using 60 MeV/nucleon ^{14}O beams. However, the energy straggling in such a target is large, and for heavier-mass projectiles, it would be unacceptably large. The excitation of the GMR in the ^{56}Ni nucleus [7] has also been reported using deuterium in the active target MAYA at the Grand Accelerateur National D'Ions Lourds (GANIL) [8].

Chen *et al.* [9] have explored the possibilities of using ^{6}Li in giant resonances studies and have shown that the inelastic scattering of ^{6}Li excites the ISGMR strongly. For ^{6}Li scattering, the low-lying particle emission threshold gives a large breakup probability into the dominant channel $^{6}\mathrm{Li} \rightarrow \alpha + d$. Therefore the contribution of multistep processes should be low especially at higher excitation energy.

With the intention of extending the study of ISGMR to unstable nuclei with inelastic scattering using a ^{6}Li target, optical parameters are needed for distorted-wave Born approximation (DWBA) calculations of multipole excitations. Therefore we are using a ^{6}Li beam on stable targets to investigate optical potentials and explore how reliable $B(E2)$ and $B(E3)$ values for well-known low-lying states are reproduced. Thus our primary focus is to obtain appropriate folding model parameters that can be used to obtain a systematic parameter set that can be used in giant resonance studies of unstable nuclei.

The mass and energy dependencies of the volume integral of the nuclear potential have been explored by several groups [10–12]. They found that the volume integral of the nuclear potential will slowly decrease as the incident energy and target mass increase. In our case, we would study giant resonances with 40 MeV/nucleon beams, so we are concerned only with the target mass dependence.

In an effort to extract a systematic optical potential for loosely bound nuclei, Trache *et al.* [13] have studied the elastic scattering of loosely bound *p*-shell nuclei and optical model parameters were obtained from the fits to the elastic-scattering angular distributions using the density-dependent JLM *NN* interaction in double-folding model calculations. Renormalization factors for both the real and imaginary part of the potentials were found to be very stable for all projectile-target systems. They suggested [13] that one can indeed obtain the optical model potentials for pairs of projectile-target nuclei for which data are not available or scarce by using a folding model procedure with renormalization factors extracted from the systematics. This procedure has been widely used in the description of elastic and transfer reactions involving stable, loosely bound *p*-shell nuclei at $E \sim$ 10–20 MeV/nucleon [14–16]. In a similar approach T. Furumoto and Y. Sakuragi [17], used the folding model with the JLM *NN* interaction for a systematic analysis of α–nucleus elastic scattering in the range of $E_{\mathrm{lab}} =$ 40–240 MeV.

The density-dependent M3Y effective *NN* interaction [18,19] has also been successfully used in a number of cases [18–21] to fit elastic-scattering data. In some studies of heavy-ion elastic scattering, it was found sufficient to treat the effective *NN* interaction as having a complex strength so that

*Present Address: Department of Chemistry, Washington University at St. Louis, St. Louis, MO 63130.

the real and imaginary optical potentials have the same radial shape [22]. However, in the analysis of refractive α-nucleus scattering [23] and of light heavy-ion scattering [24,25] an imaginary potential with a shape different from the real potential was required to reproduce elastic scattering beyond the rainbow angle. A hybrid model, where the folding model is used to calculate the real potential and a Woods-Saxon (WS) form is used for the imaginary potential has been successfully used to describe α- and heavy-ion scattering data by several authors [12,21,22,26–30]. A detailed study of the double-folding approach for α-nucleus scattering on targets in different mass regions was made by D. T. Khoa in 2001 [26].

Here we report the results of a study of elastic and inelastic scattering to low-lying states of ^{40}Ca and ^{48}Ca using 240-MeV ^{6}Li ions. Optical parameters were obtained in two ways. The elastic-scattering data were fit with cross sections calculated using the double-folding model with the density-dependent M3Y interaction and the systematics of ^{6}Li potentials from studies of ^{24}Mg, ^{28}Si, ^{58}Ni, and ^{90}Zr [21,28] were used to predict parameters for ^{40}Ca and ^{48}Ca. The differential cross sections for the low-lying 2^+ and 3^- states were also obtained, and DWBA calculations were carried out using both the "fitted" potentials and those obtained from the systematics to obtain *B(EL)* values. Differential cross sections for the excitation of giant resonances in these nuclei were also calculated using both sets of parameters.

Nadasen *et al.* [11] have studied ^{6}Li elastic scattering from ^{40}Ca at 210-MeV beam energy and fit the data with phenomenological WS potentials. Farid and Hassanain [31,32] have analyzed 210-MeV ^{6}Li scattering on ^{40}Ca using a density-independent double-folding model with both the M3Y and JLM *NN* interactions. Previous studies of ^{6}Li optical potentials for scattering from a number of other nuclei were thoroughly discussed in Ref. [28]. We have previously reported optical parameters for 240-MeV ^{6}Li scattering from ^{24}Mg and ^{28}Si [21], ^{58}Ni and ^{90}Zr [28], and ^{116}Sn [12] and, except for

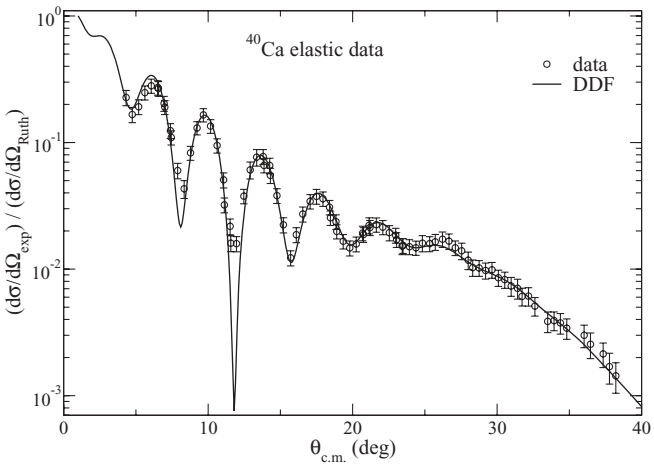

FIG. 1. The experimental angular distribution of the cross section (relative to Rutherford cross section) for ^{6}Li + ^{40}Ca elastic scattering is shown by the circles. The error bars include statistical and systematic errors. The line shows the cross section calculated with the DDF potential parameters obtained by fitting the data.

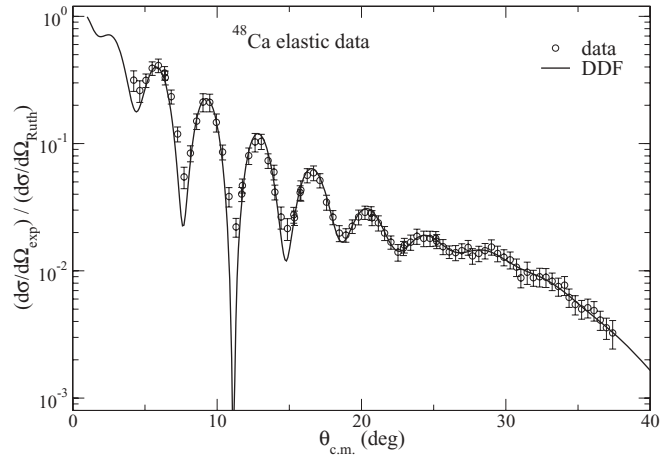

FIG. 2. Same as Fig. 1 but for ^{48}Ca.

^{116}Sn, these parameters form the basis of a systematic potential that we test in this work.

II. EXPERIMETAL TECHNIQUE

The experimental technique for the ^{6}Li-scattering measurements was similar to that for α scattering described in Ref. [30] and is summarized briefly below.

Beams of 240-MeV ^{6}Li ions from the Texas A&M K500 superconducting cyclotron bombarded self-supporting target foils (enriched to more than 95%, 5.02 mg/cm^2 ^{40}Ca and 4.4 mg/cm^2 ^{48}Ca) in the target chamber of the multipole-dipole-multipole (MDM) spectrometer [33]. The beam was delivered to the MDM spectrometer through a beam analysis system [34] to remove halo and improve momentum resolution and was stopped on a Faraday cup inside the scattering chamber. The horizontal acceptance of the spectrometer was

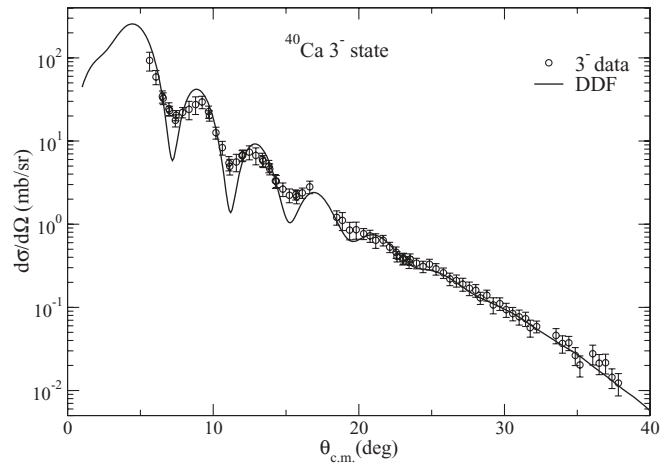

FIG. 3. The angular distribution of the differential cross section for inelastic scattering of 240 MeV ^{6}Li ions exciting the 3.737-MeV 3^- state of ^{40}Ca is shown by the circles. The error bars include statistical and systematic errors. The line shows the angular distribution obtained from the DWBA calculations with the DDF parameters, normalized to the data to obtain the lowest χ^2.

TABLE I. Parameters for the Fermi model of the ground-state density distributions used in the folding calculations.

Nucleus	ρ_0 (fm^{-3})	c (fm)	a (fm)	$\langle r^2 \rangle$ (fm)	Reference
^{40}Ca	0.169	3.60	0.523	3.399	[31]
^{48}Ca	0.187	3.723	0.515	3.479	[37]

4° and ray tracing was used to reconstruct the scattering angle. The focal-plane detector consisted of four 60-cm-long resistive wire proportional counters to measure position, an ionization chamber to measure ΔE, and a scintillator to measure E and to provide a fast timing signal for each event. The out-of-plane scattering angle (ϕ) was not measured. The principles of operation of the detector are similar to the detector described in Ref. [35]. The details of angle and position calibrations were described in Ref. [36]. A position resolution of approximately 0.9 mm and scattering angle resolution of about 0.09° were obtained.

Data for elastic scattering and inelastic scattering exciting the low-lying states were taken at spectrometer angles ranging from 4° to 40° with a spectrometer acceptance of $\Delta\theta = 4.0°$. The vertical acceptance was ±1° for spectrometer angles from 4° to 9° and ±2° for spectrometer angles from 11° to 40°. In the data analysis, data taken at one spectrometer angle were divided into 10 angle bins, each angle bin corresponding to $\Delta\theta \approx 0.4°$. The average angle for each bin was determined by averaging over the height of the solid angle defining slit and the width of the angle bin. For each angle bin, the elastic- and inelastic-scattering peak positions, widths, and cross sections were extracted by integration or by a Gaussian fitting routine. The target thicknesses were obtained by measuring the energy loss of 240-MeV α and ^{6}Li beams passing through ^{48}Ca and ^{40}Ca targets, respectively. The absolute differential cross sections for each angle bin were obtained from the combination of yield, charge integration, target thickness, solid angle, and dead-time correction. The cumulative uncertainties in target thickness, solid angle, etc., result in a ±10% uncertainty in the cross section. Data from a monitor detector, fixed at $\theta_{\rm lab} = 25°$, were used as a check on the charge integration to verify the normalization between the different data sets across the angular range. Experimental angular distributions of the cross section (relative to Rutherford cross section) for elastic-scattering data are shown in Figs. 1 and 2. The experimental angular distribution of the cross sections for excitation of the 3.737-MeV 3$^-$ state in ^{40}Ca is shown in Fig. 3 and those obtained for the 3.832-MeV 2$^+$ and 4.507-MeV 3$^-$ states of ^{48}Ca are shown in Fig. 4.

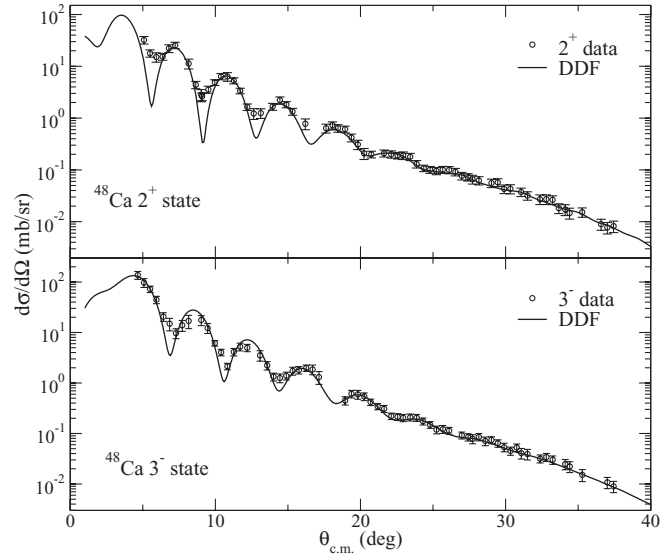

FIG. 4. The angular distribution of the differential cross sections for inelastic scattering of 240 MeV ^{6}Li ions exciting the 3.832-MeV 2$^+$ state (upper panel) and 4.507-MeV 3$^-$ state (lower panel) of ^{48}Ca are shown by the circles. The error bars include statistical and systematic errors. The lines show the angular distribution obtained from the DWBA calculations with the DDF parameters, normalized to the data to obtain the lowest χ^2.

III. RESULTS AND ANALYSIS

A. Double-folding model description of the elastic and inelastic scattering to low-lying states

In this work, we have followed the same approach as in our earlier work [28], where the real part of the potentials was calculated using the density-dependent M3Y *NN* interaction in the double- folding model and the imaginary part was calculated using a WS form. A Fermi distribution (see Table I) was used for the target ground-state density and the cluster-orbital shell-model approximation [38] form was used for the ^{6}Li ground-state density (see Eq. (8) of Ref. [12]).

TABLE II. Optical model parameters obtained from fits of elastic scattering with the density-dependent double-folding calculations using the M3Y interaction (DDF fit). N_r is the renormalization factor for the real potential. S_r is the scaling factor for the radius of the real potential. W_i, r_{i0}, and a_i are WS parameters for the imaginary potentials. J_w is the volume integral per nucleon pair for the imaginary potentials. σ_r is the total cross section of the reaction. DIF means density-independent folded potential. The asterisk means that $R_w = r_{i0}A_T^{1/3}$.

Target	E_{Li} (MeV)	*NN* int.	Potential type	N_r	S_r	W_i (MeV)	r_{i0} (fm)	a_i (fm)	J_w (MeV fm^3)	χ^2	σ_r (mb)
^{40}Ca	240 [Present]	M3Y	DDF	0.895	1.086	42.95	0.923	1.106	128	1.7	2090
	210 [31]	M3Y	DIF	0.740		32.20	1.633*	0.891	122	2.6	1940
	210 [32]	JLM	DIF	0.524		18.22	1.938*	0.659		9.6	1865
^{48}Ca	240 [Present]	M3Y	DDF	0.904	1.075	31.62	1.054	0.903	109	1.2	2021

TABLE III. *(EL)* values for 3^- state of ^{40}Ca and 2^+ and 3^- states of ^{48}Ca obtained with the double-folding model. Adopted values of *B(E2)* and *B(E3)* are also shown in the table. The errors represent total errors including statistical and systematic errors.

Work	Parameter set	^{40}Ca $J^\pi = 3^-$, $E_x = 3.737$ MeV $B(E3)$ (e^2 b^3)	^{48}Ca $J^\pi = 2^+$, $E_x = 3.832$ MeV $B(E2)$ (e^2 b^2)	^{48}Ca $J^\pi = 3^-$, $E_x = 4.507$ MeV $B(E3)$ (e^2 b^3)
	DDF	0.0179 ± 0.0018	0.0116 ± 0.0012	0.0075 ± 0.0008
	Q1	0.0164 ± 0.0017	0.0140 ± 0.0014	0.0083 ± 0.0008
	Q2	0.0171 ± 0.0017	0.0126 ± 0.0013	0.0075 ± 0.0008
Present	Q3	0.0164 ± 0.0017	0.0155 ± 0.0016	0.0105 ± 0.0011
	L1	0.0171 ± 0.0017	0.0155 ± 0.0016	0.0094 ± 0.0009
	L2	0.0164 ± 0.0017	0.0140 ± 0.0014	0.0085 ± 0.0009
	L3	0.0197 ± 0.0020	0.0155 ± 0.0016	0.0105 ± 0.0011
Adopted values		0.0184 ± 0.0020 [42]	0.0095 ± 0.0032 [43]	0.0083 ± 0.0020 [42]

Density-dependent double-folding calculations were carried out with the folding code DFPD4 [39] and DWBA calculations were done using the program ECIS [40].

The quality of fit of elastic as well as inelastic scattering is estimated by χ^2, defined by

$$\chi^2 = \frac{1}{N}\sum_{i=1}^{N}\left[\frac{\sigma(\theta_i)^{\rm cal} - \sigma(\theta_i)^{\rm exp}}{\Delta\sigma(\theta_i)}\right]^2, \qquad (1)$$

where N is the number of data points, $\sigma(\theta_i)^{\rm cal}$ is the ith calculated cross section, $\sigma(\theta_i)^{\rm exp}$ is the experimental cross section, and $\Delta\sigma(\theta_i)$ is the corresponding absolute uncertainty.

The optical potential parameters obtained from the density-dependent double-folding calculations (DDF) for ^{40}Ca and ^{48}Ca are shown in Table II. The results for ^{40}Ca are compared with those obtained by Farid and Hassanain [31,32]. The calculated angular distributions of the cross sections are plotted along with elastic-scattering data in Figs. 1 and 2.

The renormalization factors (N_r) obtained are about 0.90 for both ^{40}Ca and ^{48}Ca target nuclei. Similar values were required for other nuclei, 0.823 and 0.887 [21] for ^{24}Mg and ^{28}Si, respectively, and 0.875 and 0.878 [28] for ^{58}Ni and ^{90}Zr, respectively, using the same interaction. A somewhat lower value $N_r = 0.65$ was required to fit 240-MeV ^{6}Li scattering from ^{116}Sn [12]. Farid *et al.* [31,32] have analyzed 210-MeV ^{6}Li scattering from ^{40}Ca using double-folding calculations with the density-independent M3Y and JLM *NN* interactions.

TABLE IV. The values of renormalization factor for the real potential (N_r), scaling factor for the radius of the real potential (S_r), volume integral per nucleon pair for the imaginary potential (J_w), and depth of the imaginary part of the potential (W_i) are taken from Refs. [21,28].

Target	N_r	S_r	J_w (MeV fm^3)	W_i (MeV)	Reference
^{24}Mg	0.823	1.0620	154	58.67	[21]
^{28}Si	0.887	1.0624	136	41.33	[21]
^{58}Ni	0.875	1.0594	112	35.33	[28]
^{90}Zr	0.878	1.0661	102	33.34	[28]

In both cases the renormalization factors (N_r) are lower (see Table II) than our results with the density-dependent M3Y *NN* interaction.

A scaling factor on the radius of the real optical potential, S_r, is necessary to fit the elastic-scattering data for both ^{40}Ca (1.086) and ^{48}Ca (1.075). A similar scaling factor was required to fit data for ^{6}Li scattering from ^{24}Mg (1.062), ^{28}Si (1.0624) [21], ^{58}Ni (1.059), and ^{90}Zr (1.066) [28] target nuclei, which has been attributed to a repulsive surface correction for dynamical polarization potential [21,41].

As a further test of the optical model parameters, DWBA calculations were performed with these parameters for the low-lying 2^+ and 3^- states using these parameters, and are shown superimposed on the data in Figs. 3 and 4,

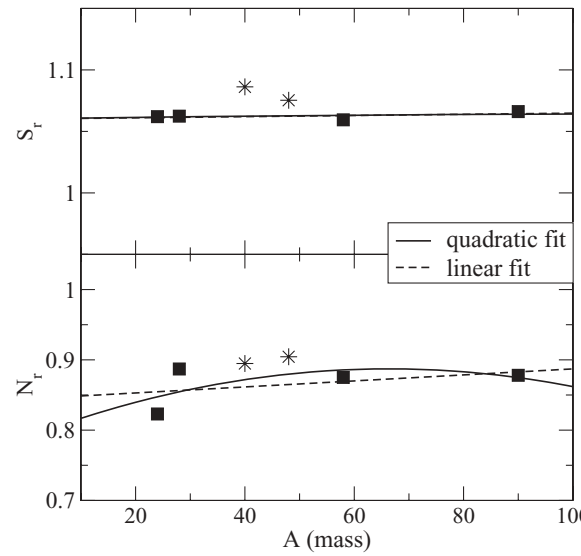

FIG. 5. The target mass number dependence of renormalization (Nr) and radius scaling (S_r) factors of the real part of the potential are shown by solid squares. The ^{24}Mg and ^{28}Si results are from Ref. [21], and the ^{58}Ni and ^{90}Zr results are from Ref. [28]. Solid and broken lines are quadratic and linear fits of the data, respectively. The stars show the results from the DDF fit to the ^{40}Ca and ^{48}Ca elastic scattering data.

normalized to the data to produce the lowest χ^2. The real parts of the transition potentials were calculated by folding the *NN* effective interaction over the densities of the target and projectile, while the imaginary parts were constructed with the deformed potential model. The transition potentials were calculated with DFPD4 [39] and the cross sections were calculated with ECIS [40]. Details of this process can be found in Refs. [12,28]. The *B(E2)* and *B(E3)* values obtained agree with the adopted values within errors and are given in Table III.

B. Systematic ^{6}Li-nucleus folding potential parameters

In order to test the effectiveness of systematic optical potentials for our studies, we have used optical potentials previously obtained for ^{24}Mg, ^{28}Si, ^{58}Ni, and ^{90}Zr to obtain optical potentials for ^{40}Ca and ^{48}Ca. We then compare elastic scattering fits, fits to low-lying states and *B(EL)* values obtained for the low-lying states, and giant resonance cross sections obtained with the two approaches.

The ^{6}Li optical parameters obtained for ^{116}Sn [12] do not follow the trend of these four lighter nuclei, and they have not been used in this study. Due to availability of suitable beams, our first studies of radioactive nuclei will be limited to lighter nuclei ($A < 40$), so that limiting this study to $A \leqslant 90$ suits the present purpose.

The real potential in these studies was obtained by double-folding using the M3Y interaction, so the target mass dependence is "built in" from the Fermi parameters for the mass distribution. However, two additional parameters were required to fit the elastic data: N_r (renormalization factor) and S_r (radial scaling factor). The values of these factors for ^{24}Mg, ^{28}Si, ^{58}Ni, and ^{90}Zr are summarized in Table IV and plotted in Fig. 5 which includes the ^{40}Ca and ^{48}Ca values from Table II. Linear and quadratic fits to the ^{24}Mg, ^{28}Si, ^{58}Ni, and ^{90}Zr points are also shown in Fig. 5. From these fits, values were obtained for ^{40}Ca ($N_r = 0.872$, $S_r = 1.062$ from quadratic fit, $N_r = 0.862$, $S_r = 1.062$ from linear fit) and for ^{48}Ca ($N_r = 0.880$, $S_r = 1.063$ from quadratic fit, $N_r = 0.865$, $S_r = 1.062$ from linear fit) to be used in the "systematic" optical potentials

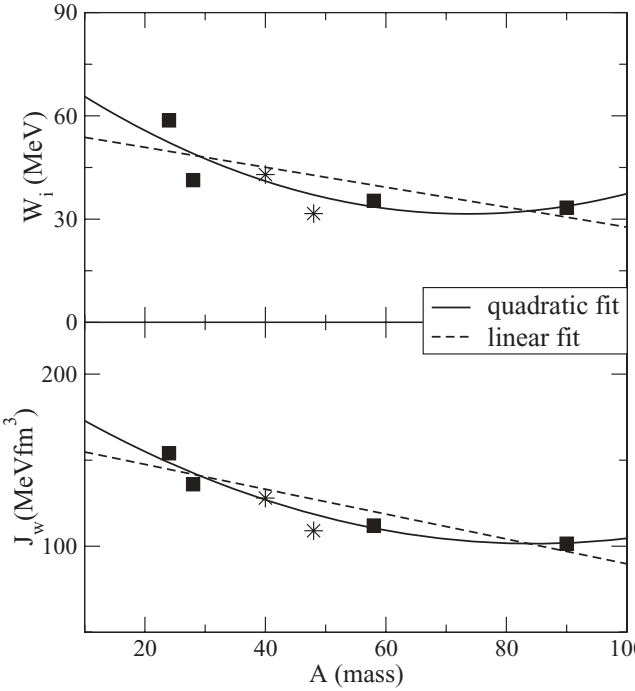

FIG. 6. The target mass number dependence of the volume integral of the imaginary part of the potential (J_w) is shown by dark squares in the bottom panel and the depth of the imaginary part of the potential (W_i) is shown by dark squares in the top panel. The ^{24}Mg and ^{28}Si results are from Ref. [21], and the ^{58}Ni and ^{90}Zr results are from Ref. [28]. Solid and broken lines are quadratic and linear fits of the data, respectively. The stars show the results from the DDF fit to the ^{40}Ca and ^{48}Ca elastic-scattering data.

TABLE V. Optical model parameters for ^{40}Ca and ^{48}Ca obtained from the systematic approach (Q1-Q3 and L1-L3) (see text). Parameters obtained by fitting the elastic scattering (DDF) are shown for comparison.

Target	label	N_r	S_r	W_i (MeV)	r_{i0} (fm)	a_i (fm)	J_w (MeV fm^3)	χ^2	σ_r (mb)
	DDF	0.895	1.086	42.95	0.923	1.106	128	1.7	2090
	Q1			41.04	0.942	1.085		2.8	2074
	Q2	0.872	1.062	47.25	0.869	1.152	127	9.2	2100
^{40}Ca	Q3			36.25	1.001	1.048		2.9	2091
	L1			45.07	0.898	1.183		2.9	2214
	L2	0.862	1.062	50.06	0.839	1.246	133	4.9	2255
	L3			40.06	0.943	1.195		3.6	2287
	DDF	0.904	1.075	31.62	1.054	0.903	109	1.2	2021
	Q1			37.05	0.997	1.062		2.9	2239
	Q2	0.880	1.063	42.05	0.948	1.052	119	2.6	2155
^{48}Ca	Q3			32.05	1.064	1.025		7.6	2274
	L1			42.78	0.949	1.134		5.3	2335
	L2	0.865	1.062	47.78	0.909	1.116	127	3.0	2252
	L3			37.78	1.008	1.098		9.4	2354

for these nuclei. These differ somewhat from those obtained by the DDF fits to the elastic scattering (Table II).

The mass dependence of the volume integrals of the imaginary part of optical potentials (J_w's) [21,28], defined as:

$$J_w = \frac{1}{A_T A_P} \int w(r) d\tau, \tag{2}$$

where $w(r)$ is the imaginary part of the optical potential and A_T and A_P are the mass numbers of the target and the projectile, is shown in the bottom panel of Fig. 6. Their behavior is consistent with other works [10–12] where it was found that the volume integral of the nuclear potential slowly decreases as the target mass increases. Quadratic and linear fits to the ^{24}Mg, ^{28}Si, ^{58}Ni, and ^{90}Zr points are also shown. Values of J_w for ^{40}Ca (127 and 133 MeV fm^3) and ^{48}Ca (119 and 127 MeV fm^3) were extracted from the quadratic and linear fits, respectively. The values for ^{40}Ca are close to that obtained from the DDF fits (128 MeV fm^3) but for ^{48}Ca are substantially higher than that from the DDF fit (109 MeV fm^3).

Unfortunately, the WS parameters used in DWBA calculations are not uniquely determined by J_w, which is the volume integral of the potential, as defined in Eq. (2). In order to obtain realistic values of W_i, r_{i0}, and a_{i0}, a systematic approach for these parameters is required. The mass dependence of the depth of the imaginary part of the potential (W_i) obtained for 240-MeV ^{6}Li scattering data [21,28], is plotted in the upper panel of Fig. 6. Quadratic and linear fits to the values for ^{24}Mg, ^{28}Si, ^{58}Ni, and ^{90}Zr are also shown. Values of W_i for ^{40}Ca (41.04 and 45.07 MeV) and ^{48}Ca (37.05 and 42.78 MeV) were extracted from the quadratic and linear fits, respectively. Using these values of W_i corresponding values of r_{i0} and a_{i0} were extracted, keeping the values of J_w constant. These sets are labeled as L1 and Q1 for linear and quadratic fits in Table V.

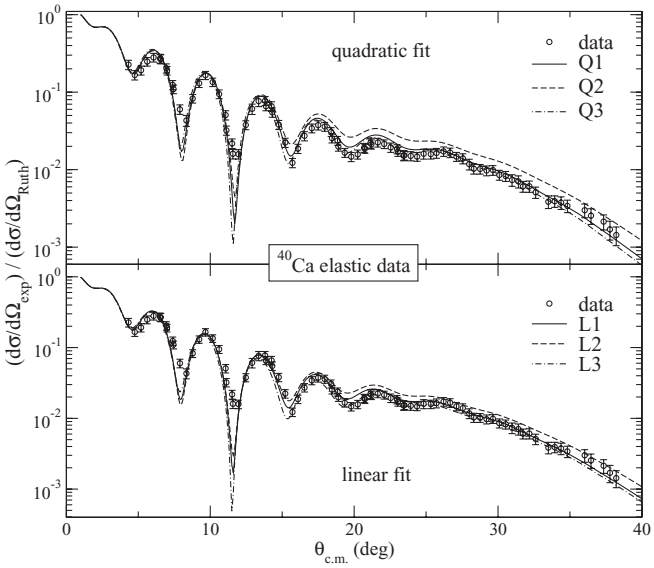

FIG. 7. The angular distribution of the cross sections (relative to Rutherford cross section) calculated with Q1-Q3 and L1-L3 sets of parameters (see text for detail) are plotted along with the data for ^{6}Li+^{40}Ca elastic scattering.

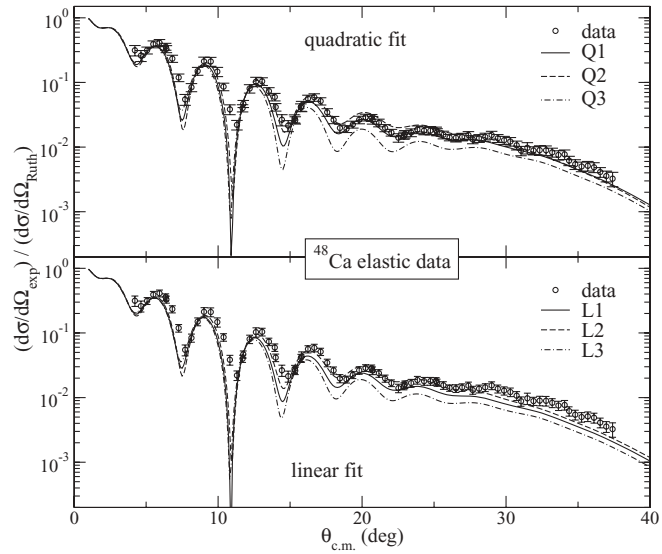

FIG. 8. Same as Fig. 7 but for ^{48}Ca.

1. Elastic and inelastic scattering to low-lying states

The cross sections for elastic scattering obtained with these sets of parameters (Q1 and L1) are compared with the data in Figs. 7 and 8 and the χ^2 values obtained are shown in Table V. Although the quality of fit is still good for ^{40}Ca, the χ^2 values are about 50% larger using the parameters from both the linear and quadratic fits than from the DDF calculations. For ^{48}Ca, at larger angles the cross sections calculated with the parameters from the quadratic fit are obviously below the data and the χ^2 value is more than twice that obtained with the DDF calculations. The cross sections calculated for ^{48}Ca with the parameters from the linear fit are even further below

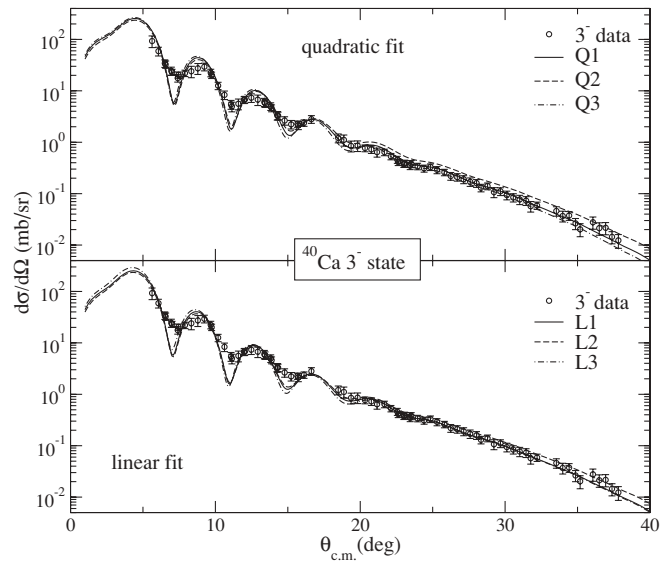

FIG. 9. The angular distributions of the differential cross sections calculated with the parameters Q1-Q3 and L1-L3 (see text for detail) for inelastic scattering to the 3.737-MeV 3$^-$ state of ^{40}Ca are plotted along with the data.

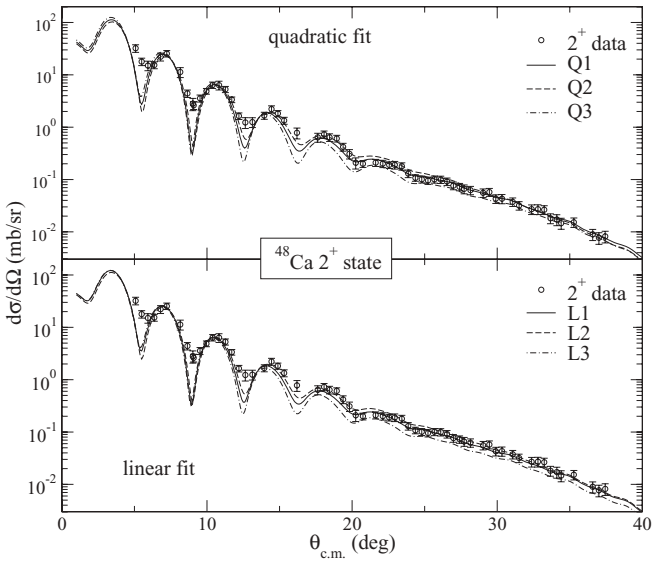

FIG. 10. The angular distributions of the differential cross sections calculated with the parameters Q1-Q3 and L1-L3 (see text for detail) for inelastic scattering to the 3.832-MeV 2^+ state of ^{48}Ca are plotted along with the data.

the data at large angles and the χ^2 value obtained are about a factor of 4.5 larger than with the DDF calculations.

As a further test of the optical model parameters obtained from the systematics, DWBA calculations using the double-folding model with Q1 and L1 sets of parameters were made for the 3.737-MeV 3^- state of ^{40}Ca and the 3.832-MeV 2^+ and the 4.507-MeV 3^- states of ^{48}Ca and are shown superimposed on the data in Figs. 9–11, normalized to produce the lowest χ^2.

B(EL) values obtained from the fits, Q1 and L1, are listed in Table III. The associated error represents the total error including both statistical and systematic errors (including the error in the absolute cross section). The results are compared

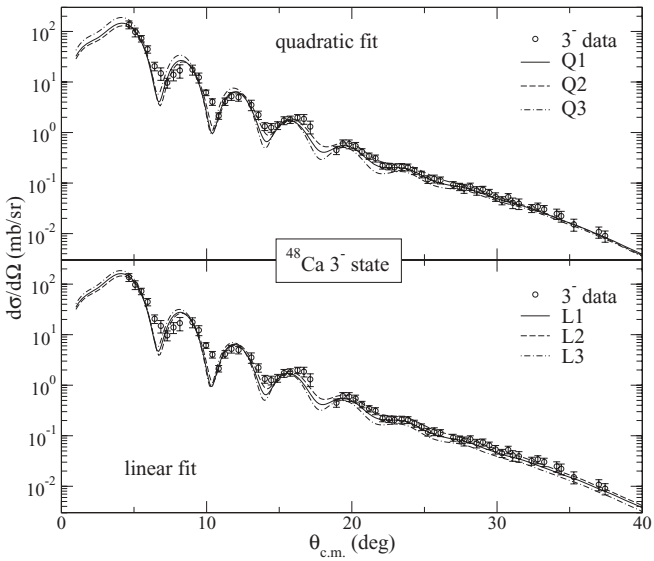

FIG. 11. Same as Fig. 10 but for the 4.507-MeV 3^- state of ^{48}Ca.

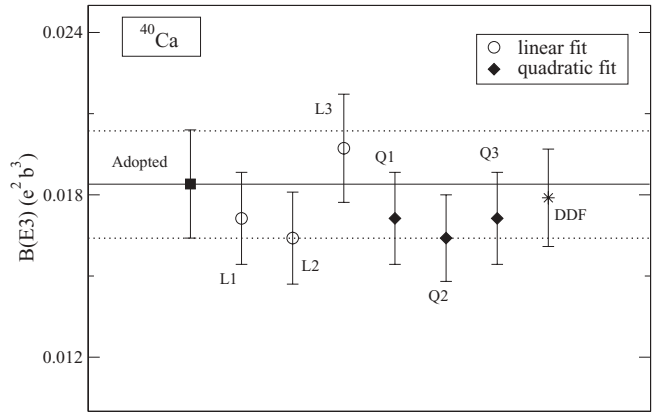

FIG. 12. $B(E3)$ values for the 3^- state in ^{40}Ca, obtained with the different sets of parameters are compared with the adopted values.

with those obtained with DDF fit and the adopted $B(E2)$ [43] and $B(E3)$ [42] values in Table III and in Figs. 12 and 13. The $B(E3)$ values for the 3^- states in ^{40}Ca and ^{48}Ca obtained with Q1 and L1 sets of parameters agree with the adopted values as well as with those obtained with DDF fit. The $B(E2)$ value for the 2^+ state in ^{48}Ca obtained with Q1 agrees within error with the adopted value. The corresponding value obtained with L1 is higher that the adopted value.

It has been suggested [24,44] that optical parameters that have the same volume integral will result in similar predictions for cross sections. In order to test this, we varied the value of W_i (obtained originally from the systematics illustrated in the top panel of Fig. 6), keeping J_w constant. Values of W_i's were varied approximately by ± 5 MeV and then corresponding values of r_{i0} and a_{i0} were extracted by requiring that J_w remain constant. These set of parameters are labeled as Q2 and Q3 and L2 and L3 for the quadratic and linear fits, respectively. The renormalization and radial scaling factors were kept the same as for the L1 and Q1 sets. Differential cross sections for elastic scattering were calculated using these sets of parameters and are plotted in Figs. 7 and 8. From these figures and Table V, we see that for ^{40}Ca, sets Q3 and L3 (in which W_i's have been

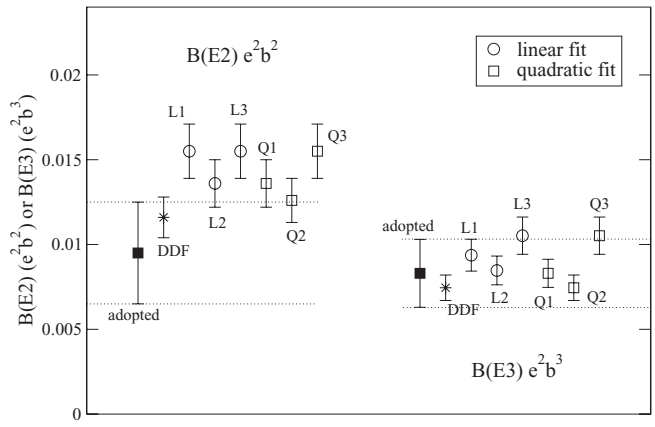

FIG. 13. $B(E2)$ and $B(E3)$ values, obtained using different sets of parameters, for the 2^+ and 3^- states of ^{48}Ca are plotted and compared with those of adopted values.

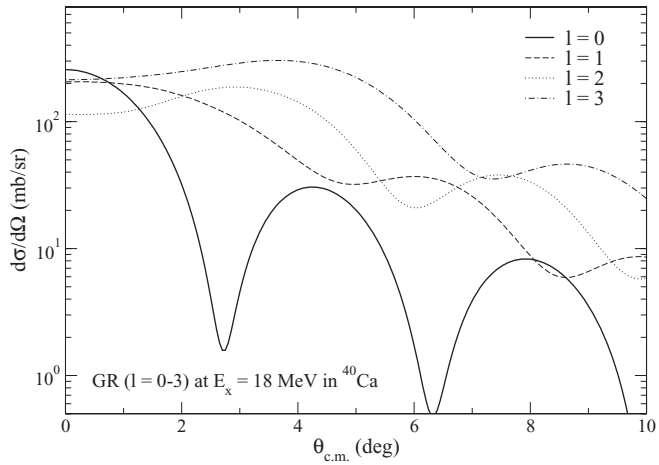

FIG. 14. Angular distributions of the differential cross section for 240-MeV ^{6}Li inelastic scattering from ^{40}Ca for $l = 0$–3 for 100% of the EWSR at $E_x = 18$ MeV.

decreased by ∼5 MeV) agree with the data fairly well and have χ^2 values within a factor of 2 of the DDF fits, whereas sets Q2 and L2 give very large χ^2 (∼6–8 times greater than that obtained with DDF fit) and do not fit data at larger angles. For ^{48}Ca, the situation is reversed. Here, sets Q2 and L2 (in which W_i's have been increased by ∼5 MeV) result in χ^2 values substantially lower than those from Q1 and L1 (see Fig. 8 and Table. V). The set of parameters Q3 and L3 predict angular cross sections far below the data, specially at larger angles. By varying the value of W_i (obtained from systematics), we found no systematic patterns in the prediction of the cross sections for ^{40}Ca and ^{48}Ca.

DWBA calculations with Q2-Q3 and L2-L3 sets of parameters were also made for the low-lying states of ^{40}Ca and ^{48}Ca and are shown in Figs. 9–11, normalized to produce the lowest χ^2. *B(EL)* values obtained with these fits are also shown in Table III and plotted in Figs. 12 and 13. *B(EL)* values, obtained with the parameters (Q2-Q3 and L2-L3) agree with adopted

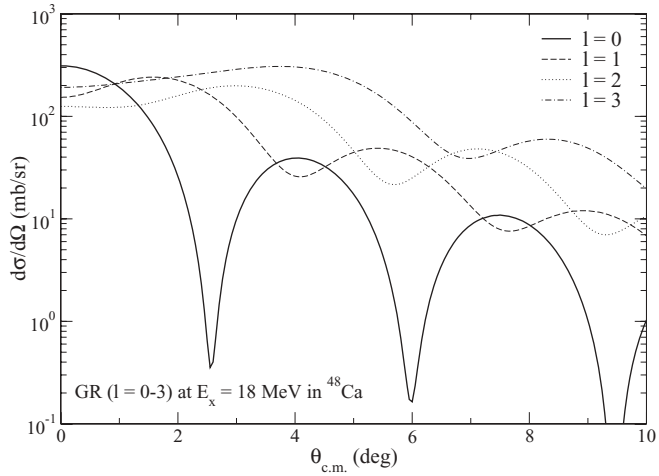

FIG. 15. Angular distributions of the differential cross section for 240-MeV ^{6}Li inelastic scattering from ^{48}Ca for $l = 0$–3 for 100% of the EWSR at $E_x = 18$ MeV.

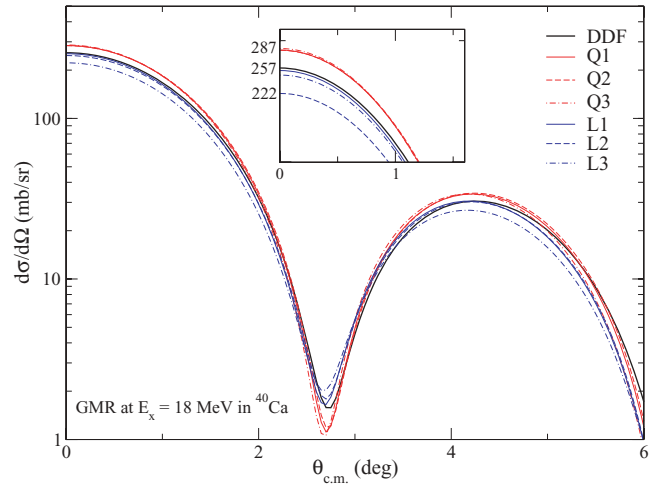

FIG. 16. (Color online) Angular distributions of the differential cross section for 240-MeV ^{6}Li inelastic scattering from ^{40}Ca for $l = 0$ (monopole resonance) for 100% of the EWSR at $E_x = 18$ MeV. The inset has the vertical scale expanded to show the region close to 0°.

values within error. The *B(E2)* values for the 2^+ state in ^{48}Ca obtained with the parameter sets L3 and Q3 are higher than the adopted value (see Fig. 13).

2. *Calculations for giant resonances*

Figures 14 and 15 show calculated differential cross sections for the excitation of various giant resonances (l = 0 to 3) in ^{40}Ca and ^{48}Ca, respectively, assuming that these resonances exhaust 100% of the respective energy weighted sum rule's (EWSR) [9]. The calculations were done for resonances at $E_x = 18$ MeV using ECIS [40] with the DDF set of parameters obtained by fitting the elastic scattering. The peak cross sections for the monopole resonances at 0° in these nuclei are found to be comparable with ^{24}Mg, ^{28}Si, and ^{116}Sn nuclei [9,21] and are adequate for studies with unstable

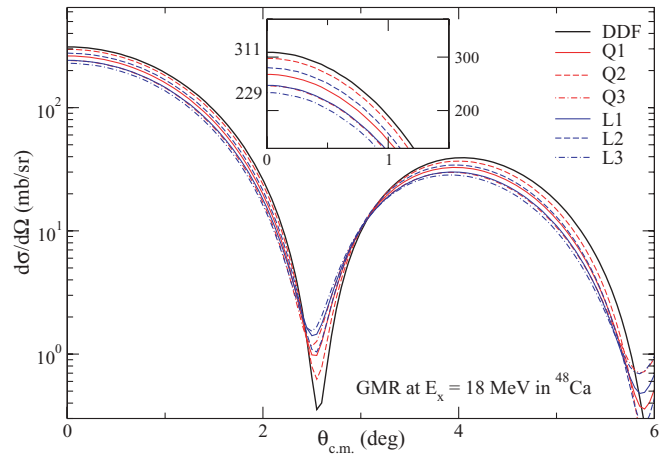

FIG. 17. (Color online) Angular distributions of the differential cross section for 240-MeV ^{6}Li inelastic scattering from ^{48}Ca for $l = 0$ (monopole resonance) for 100% of the EWSR at $E_x = 18$ MeV. The inset has the vertical scale expanded to show the region close to 0°.

beams. The ISGMR cross section decreases rapidly beyond 1°, whereas the other multipoles are basically flat or slowly varying, so that ISGMR strength should be separable from the other multipoles.

The differential cross sections for the monopole resonances in ^{40}Ca and ^{48}Ca were calculated with the parameters obtained from the systematics and are compared with those obtained with DDF parameters in Figs. 16 and 17. The peak cross sections for the monopole resonance at 0° in ^{40}Ca calculated using sets L1 and Q1 are 253 and 284 mb/sr, respectively, and are close to the value = 257 mb/sr obtained with DDF parameters (with ∼12% more for Q1 case). In the case of ^{48}Ca, the peak cross sections for monopole resonance at 0° are 263 and 242 mb/sr with parameters sets Q1 and L1, which are around ∼15 and 22% less than that obtained with DDF parameters (311 mb/sr). The calculations using parameters of sets L2, L3, Q2, and Q3 varied from those obtained with the DDF parameters by as much as 30%.

IV. CONCLUSION

Elastic and inelastic scattering of 240-MeV ^{6}Li particles from ^{40}Ca and ^{48}Ca were measured with the MDM spectrometer. Optical parameters were obtained from the fit of elastic-scattering data using double folding with the density-dependent M3Y *NN* interaction. *B(EL)* values obtained from the double-folding model agree well with adopted values for low-lying 2^+ and 3^- states. Optical parameters for ^{40}Ca and ^{48}Ca were also obtained from both linear and quadratic fits to those for ^{24}Mg, ^{28}Si, ^{58}Ni, and ^{90}Zr and the effects of varying the imaginary potential depth while retaining the volume integral constant were explored. The χ^2 values obtained for the fits to elastic scattering using the "systematic" potentials were 50–100% higher but visually would still be described as good fits. The *B(EL)* values obtained for the low-lying 2^+ and 3^- states using the parameters obtained from the quadratic fit all agreed with the adopted values within errors. Differential cross sections for the excitation of giant resonances in these nuclei were also calculated with the parameters obtained from the systematic approach as well as from the fits of elastic data. The cross sections obtained for the giant monopole resonance at 0° with the parameters from the quadratic fit to the parameters from the other nuclei agreed within 10% for ^{40}Ca and 15% for ^{48}Ca with those calculated using optical parameters obtained from fitting the elastic-scattering data. These results suggest that for nuclei between $A = 24$ and $A = 90$, optical potentials for 40 MeV/nucleon ^{6}Li scattering can be obtained for unstable nuclei using the systematic behavior of those for ^{24}Mg, ^{28}Si, ^{40}Ca, ^{48}Ca, ^{58}Ni, and ^{90}Zr without inducing unacceptable error in *B(EL)* values or giant monopole resonance strengths.

ACKNOWLEDGMENTS

This work was supported in part by the US Department of Energy under Grant DE-FG02–93ER40773 and by the Robert A. Welch Foundation under Grant A-0558.

[1] D. H. Youngblood, H. L. Clark, and Y.-W. Lui, Phys. Rev. Lett. **82**, 691 (1999).
[2] S. Shlomo, V. Kolomietz, and G. Colò, Eur. Phys. J. A **30**, 23 (2006); H. Sagawa, S. Yoshida, Guo-Mo Zeng, Jian-Zhong Gu, and Xi-Zhen Zhang, Phys. Rev. C **76**, 034327 (2007); M. Centelles, X. Roca-Maza, X. Vinas, and M. Warda, Phys. Rev. Lett. **102**, 122502 (2009).
[3] J. Piekarewicz, Phys. Rev. C **66**, 034305 (2002); **76**, 031301 (2007).
[4] D. H. Youngblood, Y.-W. Lui, B. John, Y. Tokimoto, H. L. Clark, and X. Chen, Phys. Rev. C **69**, 054312 (2004).
[5] T. Li *et al.*, Phys. Rev. Lett. **99**, 162503 (2007).
[6] H. Baba *et al.*, Nucl. Phys. A **788**, 188 (2007).
[7] C. Monrozeau *et al.*, Nucl. Phys. A **788**, 182 (2007); Phys. Rev. Lett. **100**, 042501 (2008).
[8] C. E. Demonchy, Ph.D. thesis, Université Caen, France, 2003.
[9] X. Chen, Y.-W. Lui, H. L. Clark, Y. Tokimoto, and D. H. Youngblood, Phys. Rev. C **79**, 024320 (2009).
[10] S. Gupta and K. Murthy, Z. Phys. A **307**, 187 (1982).
[11] A. Nadasen, M. McMaster, M. Fingal, J. Tavormina, P. Schwandt, J. S. Winfield, M. F. Mohar, F. D. Becchetti, J. W. Jänecke, and R. E. Warner, Phys. Rev. C **39**, 536 (1989).
[12] X. Chen, Y.-W. Lui, H. L. Clark, Y. Tokimoto, and D. H. Youngblood, Phys. Rev. C **76**, 054606 (2007).
[13] L. Trache, A. Azhari, H. L. Clark, C. A. Gagliardi, Y.-W. Lui, A. M. Mukhamedzhanov, R. E. Tribble, and F. Carstoiu, Phys. Rev. C **61**, 024612 (2000).
[14] A. Banu *et al.*, Phys. Rev. C **79**, 025805 (2009).
[15] X. Tang, A. Azhari, C. A. Gagliardi, A. M. Mukhamedzhanov, F. Pirlepesov, L. Trache, R. E. Tribble, V. Burjan, V. Kroha, and F. Carstoiu, Phys. Rev. C **67**, 015804 (2003).
[16] G. Tabacaru *et al.*, Phys. Rev. C **73**, 025808 (2006).
[17] T. Furumoto and Y. Sakuragi, Phys. Rev. C **74**, 034606 (2006).
[18] D. T. Khoa, G. R. Satchler, and W. von Oertzen, Phys. Rev. C **56**, 954 (1997).
[19] D. T. Khoa and W. von Oertzen, Phys. Lett. B **304**, 8 (1993).
[20] D. T. Khoa, W. von Oertzen, and H. G. Bohlen, Phys. Rev. C **49**, 1652 (1994).
[21] X. Chen, Y.-W. Lui, H. L. Clark, Y. Tokimoto, and D. H. Youngblood, Phys. Rev. C **80**, 014312 (2009).
[22] D. T. Khoa and G. R. Satchler, Nucl. Phys. A **668**, 3 (2000).
[23] G. R. Satchler and D. T. Khoa, Phys. Rev. C **55**, 285 (1997).
[24] M. E. Brandan and G. R. Satchler, Phys. Rep. **285**, 143 (1997) and references therein.
[25] M. E. Brandan and K. W. McVoy, Phys. Rev. C **55**, 1362 (1997).
[26] D. T. Khoa, Phys. Rev. C **63**, 034007 (2001).
[27] D. T. Khoa, W. von Oertzen, H. G. Bohlen, and S. Ohkubo, J. Phys. G **34**, R111 (2007).
[28] Krishichayan, X. Chen, Y.-W. Lui, Y. Tokimoto, J. Button, and D. H. Youngblood, Phys. Rev. C **81**, 014603 (2010).
[29] Y.-W. Lui, D. H. Youngblood, H. L. Clark, Y. Tokimoto, and B. John, Phys. Rev. C **73**, 014314 (2006).
[30] D. H. Youngblood, Y.-W. Lui, and H. L. Clark, Phys. Rev. C **60**, 014304 (1999).

[31] M. El-Azab Farid and M. A. Hassanain, Nucl. Phys. A **678**, 39 (2000).
[32] M. El-Azab Farid and M. A. Hassanain, Nucl. Phys. A **697**, 183 (2002).
[33] D. M. Pringle, W. N. Catford, J. S. Winfield, D. G. Lewis, N. A. Jelley, K. W. Allen, and J. H. Coupland, Nucl. Instrum. Methods Phys. Res. A **245**, 230 (1986).
[34] D. H. Youngblood and J. D. Bronson, Nucl. Instrum. Methods Phys. Res. A **361**, 37 (1995).
[35] D. H. Youngblood, Y.-W. Lui, H. L. Clark, P. Oliver, and G. Simler, Nucl. Instrum. Methods Phys. Res. A **361**, 539 (1995).
[36] D. H. Youngblood, Y.-W. Lui, and H. L. Clark, Phys. Rev. C **55**, 2811 (1997).
[37] G. Fricke, C. Bernhardt, K. Heilig, L. A. Schaller, L. Schellenberg, E. B. Shera, and C. W. De Jager, At. Data Nucl. Data Tables **60**, 177 (1995).
[38] A. A. Korsheninnikov, E. Y. Nikolskii, C. A. Bertulani, S. Fukuda, T. Kobayashi, E. A. Kuzmin, S. Momota, B. G. Novatskii, A. A. Ogloblin, and E. A. A. Ozawa, Nucl. Phys. A **617**, 45 (1997).
[39] D. T. Khoa (unpublished).
[40] J. Raynal, ECIS code (unpublished); in Proceedings of the Workshop on Applied Nuclear Theory and Nuclear Model Calculations for Nuclear Technology Application, Trieste, Italy, 1988.
[41] D. T. Khoa (private communication).
[42] T. Kibédi and R. H. Spear, At. Data Nucl. Data Tables **80**, 35 (2002).
[43] S. Raman, C. W. Nestor, and P. Tikkanen, At. Data Nucl. Data Tables **78**, 1 (2001).
[44] G. R. Satchler, *Direct Nuclear Reactions* (Oxford University Press, New York, 1983).